4.2 RAPID FORCING OF THE SURFACE AND NEAR-SURFACE ATMOSPHERE

Edgar L Andreas[*1], Cathleen A. Geiger[1], Kerry J. Claffey[1],
George Treviño[2], and Charles C. Ryerson[1]

[1]U.S. Army Cold Regions Research and Engineering Laboratory, Hanover, New Hampshire
[2]CHIRES, Inc, San Antonio, Texas

1. INTRODUCTION

Meteorologists and even casual observers have long recognized the drastic changes in near-surface meteorological conditions that occur during sunrise and sunset transitions. The near-surface wind speed, temperature, and relative humidity are all likely to change abruptly.

Figure 1 demonstrates how extreme such changes can be. This figure shows the refractive index structure parameter, C_n^2, measured with a red laser propagating within a few meters of the surface over a path of 182 m. Because C_n^2 is related to the turbulent fluctuations in air temperature, it is also an indicator of the sensible heat flux at the surface. The dramatic decreases in C_n^2—and thus in the magnitude of the sensible heat flux—during sunrise and sunset transitions are obvious features in Fig. 1. Other near-surface variables also change significantly during these transitions.

But the surface and the near-surface air also respond to many less predictable transitions during any given day. When clouds invade a clear sky during daylight hours, changes in the near-surface meteorology like those at sunset will occur. Alternatively, if the sky clears, the surface should respond much as it does around sunrise. The longwave forcing at the surface also changes significantly when cloud conditions change, and the near-surface meteorological conditions likewise respond.

In April 2005, we conducted a two-week experiment during which we collected surface and near-surface meteorological data with which we can study the rapid forcing of the surface by sun and clouds. Our sampling was necessarily quite fast—1 Hz for most instruments and 10 Hz for six turbulence sensors. Our analysis likewise will necessarily depart from standard surface-layer analyses based on Monin-Obukhov similarity theory, which assumes stationary conditions and formulates statistics from long averages. Rather, we recognize that near-surface conditions are generally nonstationary. Studying the rapid forcing of the surface and the atmospheric surface layer therefore requires that we quantify the nonstationarity. Here, we describe our experimental set-up, discuss two interesting cases of rapid forcing, and preview our analysis techniques, which include a new method for deciding when conditions are stationary and nonstationary.

2. MEASUREMENTS

Our measurements took place in a mowed field in rural Lebanon, New Hampshire, in April 2005. To investigate the coupling among meteorological variables in a system that was experiencing rapid atmospheric and solar forcing, we deployed a variety of near-surface instruments.

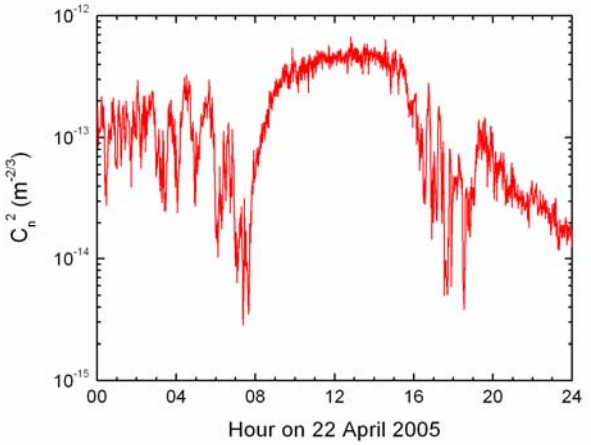

Figure 1. Samples every minute on 22 April 2005 of the refractive index structure parameter, C_n^2, obtained from a red laser propagating over a path 182 m long.

[*]*Corresponding author address:* Edgar L Andreas, U.S. Army Cold Regions Research and Engineering Laboratory, 72 Lyme Road, Hanover, New Hampshire 03755-1290; e-mail: eandreas@crrel.usace.army.mil.

Table 1. Instruments in place during our April 2005 field experiment.

Instrument	Measures	Sampling Interval (s)	Location
ATI K-type sonic anemometer/thermometer	Turbulent wind vector (u, v, w) and temperature (t)	0.1	Turbulence tower at 3.59 m
LI-COR 7500 open-path analyzer	Turbulent fluctuations in H_2O and CO_2; barometric pressure	0.1	Turbulence tower at 3.23 m
Uplooking Eppley Precision Spectral Pyranometer (PSP)	Incoming shortwave radiation	1	Radiometer mast at 1.55 m
Downlooking Eppley Precision Spectral Pyranometer (PSP)	Reflected shortwave radiation	1	Radiometer mast at 1.40 m
Uplooking Eppley Precision Infrared Radiometer (PIR)	Incoming longwave radiation	1	Radiometer mast at 1.55 m
Downlooking Eppley Precision Infrared Radiometer (PIR)	Emitted longwave radiation	1	Radiometer mast at 1.40 m
Uplooking Heitronics KT 19.85 II infrared thermometer	Sky temperature	1	Height of 1.38 m
Downlooking Heitronics KT 19.81 II infrared thermometer	Infrared surface temperature	1	Height of 0.96 m
General Eastern 1200 MPS dew-point hygrometer	Air temperature and dew-point temperature	1	Radiometer mast at 2.34 m
FLIR Systems S60 infrared camera	Image of infrared surface temperature	60	Image of 1×1 m
Scintec SLS20 Surface Layer Scintillometer	Refractive index structure parameter (C_n^2) and inner scale (ℓ_0)	60	182-m propagation path at height of 2.44 m
Nikon Coolpix 4500 digital camera, with Nikon Fisheye Converter lens FC-E8	All-sky photos	Periodically	Height of 1.98 m

More importantly, we sampled these faster than may be common for traditional meteorological observations, and we saved all these raw data.

Table 1 lists our instruments, identifies their locations and the variables they provided, and notes their sampling rates. Figure 2 shows the layout of our experimental site. Winds in the spring at this site are predominantly from southwest through northwest. We laid out the site so that our scintillometer and turbulence instruments would have unobstructed exposure for these wind directions.

Because one of our experimental objectives was to study the forcing by sun and clouds and the surface's response (cf. Roth and Oke 1995), we had multiple and redundant radiation sensors. We used standard Eppley hemispherical pyranometers and pyrgeometers to measure incoming shortwave and longwave ($Q_{L\downarrow}$) radiation, reflected shortwave radiation, and emitted longwave radiation ($Q_{L\uparrow}$). We also used Heitronics infrared thermometers—one pointed up and one pointed down—to measure sky temperature and infrared surface temperature, respectively. In contrast to the hemispherical Eppleys, the Heitronics thermometers have a very narrow field of view, about 2.5°.

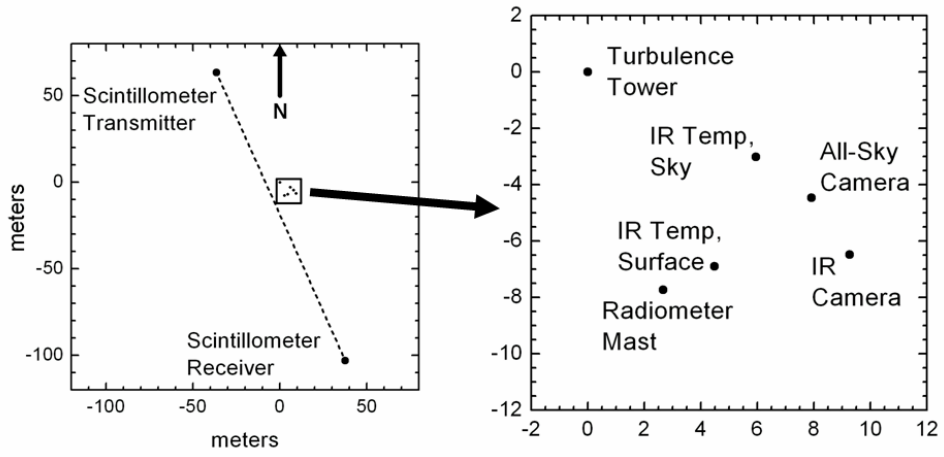

Figure 2. Instrument layout for our April 2005 experiment. The "Turbulence Tower" is at the origin of our experimental grid.

Later, we will compare Eppley longwave radiometers with the Heitronics temperatures by converting the Eppley Q_L values to a blackbody temperature using

$$T_{BB} = \left(Q_L / \sigma\right)^{0.25} \quad . \tag{1}$$

This gives T_{BB} in kelvins when Q_L is in $\mathrm{W\,m^{-2}}$, where σ $(=5.670400\times10^{-8}\,\mathrm{W\,m^{-2}\,K^{-4}})$ is the Stefan-Boltzmann constant.

Our final radiation sensor was a digital infrared camera. With this, we imaged a patch of the grass surface approximately 1 meter square every minute. Averaging temperatures over the infrared image will give us a third estimate of the radiative surface temperature. But the individual images also reveal the fine structure of the surface temperature field. Only recently has the microscale spatial variability of surface temperature been documented and recognized as an important constraint on surface-layer similarity theory (Kukharets and Tsvang 1998; Andreas et al. 1998).

This infrared camera also has a digital camera mode. Figure 3 shows nearly simultaneous visible and infrared images from this camera to highlight how wildly the blackbody temperature of a surface can vary over a small area. On comparing the visible and infrared images in Fig. 3, we see that, in general, the dead grass is relatively warm while the green grass is cool; and the range in blackbody temperatures over this small patch is 7°C.

To observe the turbulence at our site, we used a K-type sonic anemometer/thermometer made by Applied Technologies, Inc. (ATI; Kaimal et al. 1990; Kaimal and Gaynor 1991; Kaimal and Finnigan 1994, p. 218f.). This measures the three components of the turbulent velocity vector, u, v, and w, and the turbulent temperature fluctuations, t. Later, we will show plots of the wind speed, which we compute as

$$s = \left(u^2 + v^2 + w^2\right)^{1/2} \quad . \tag{2}$$

Near the sonic, but below it (Kristensen et al. 1997), we placed a LI-COR 7500 gas analyzer, which measures the turbulent fluctuations in water vapor and carbon dioxide at 10 Hz. Eventually, we will combine these data with the sonic measurements to compute the turbulent fluxes of momentum, sensible heat, latent heat, and carbon dioxide.

To tie our point measurements together with longer spatial scales, we lastly deployed a Scintec surface layer scintillometer system that propagated a red laser over a 182-m path at a nominal height of 2.44 m. Our main instrument cluster was near the center of the propagation path (Fig. 2). This scintillometer is another turbulence instrument (e.g., Thiermann 1992; De Bruin et al. 2002; Andreas et al. 2003). At the transmitter, a beam splitter divides the laser into two beams; the receiver unit likewise has two receivers. The intensity fluctuations in the laser light received at either receiver yield the refractive

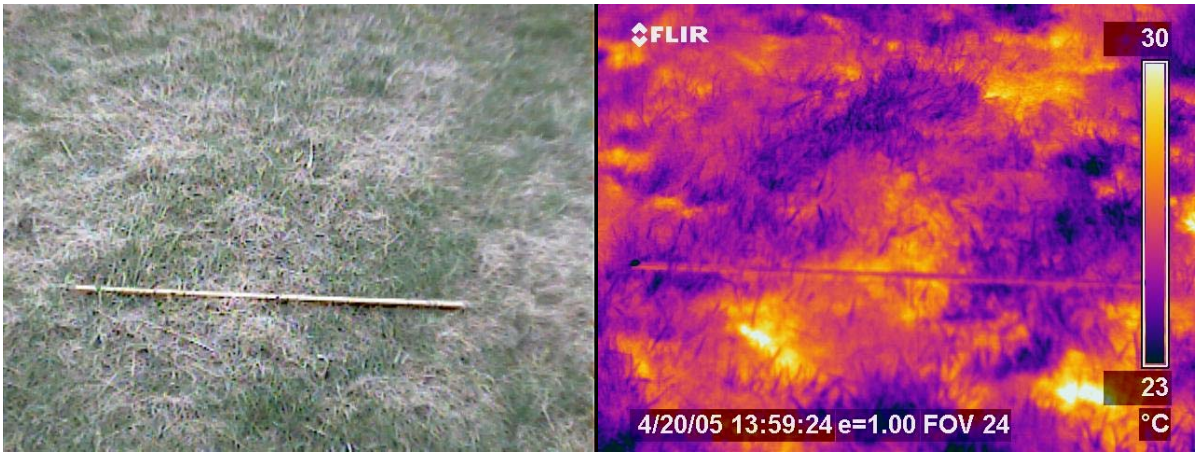

Figure 3. Visible and infrared images from our infrared camera at 1:59 p.m. on 20 April 2005. A meter stick in both images shows the scale. The emissivity for every pixel in the infrared scene is assumed to be 1.00.

index structure parameter, C_n^2. The correlation in intensity fluctuations between the two receivers provides the inner scale of turbulence, ℓ_0 (Thiermann 1992; Hill 1992), which is, in turn, related to the dissipation rate of turbulent kinetic energy (Hill and Clifford 1978). Together, C_n^2 and ℓ_0 can provide path-averaged estimates of the turbulent momentum and sensible heat fluxes (Andreas 1989, 1991, 1992; Hill et al. 1992; De Bruin et al. 2002). Figure 1 is an example of C_n^2 values from this instrument.

3. EXAMPLES OF RAPID FORCING

In this preliminary report on our experiment, we focus on just two contrasting days. April 15 (Fig. 4) had clear skies during daylight hours and represents the type of canonical good weather that boundary layer meteorologists have sought to satisfy the assumption of stationarity (e.g., Wyngaard 1973). April 26 (Fig. 5), on the other hand, had thick clouds during the night, a few hours of clearing skies before sunrise, variable cloudiness during the day, and clearing skies again after sunset. Figures 4 and 5 show time series from several of our instruments for the entire days of April 15 and 26.

With the clear skies of April 15 (Fig. 4), several of the time series follow the solar forcing (i.e., “Shortwave In”). The “Surface” temperature, for example, shows almost the same sinusoidal shape as the “Shortwave In”. The increasing fluctuations in the ”Surface” temperature toward solar noon and the decreasing fluctuations after noon correlate with the fluctuations in “Air” temperature and wind speed. In fact, both the trend in wind speed during daylight and the turbulent fluctuations about this trend also follow the solar sinusoid. The trace of refractive index structure parameter, C_n^2, also shows a clear response to the solar forcing. It has deep minima within 30 minutes of sunrise and sunset that also correlate with minima in the magnitude of the fluctuations in “Air” temperature.

The radiative “Sky” and “Surface” temperatures in Fig. 4 provide good evidence that the sky was basically clear this entire day. The difference between these temperatures of at least 20°C and the absence of much variability in the “Sky” temperature are signatures of cloudless skies.

Compare some of these traces with similar ones in Fig. 5, from April 26, which was a mostly cloudy day. Between midnight and 0400 hours, the three radiative temperatures, “Surface”, “Sky”, and “IR Sky”, are almost the same because of thick clouds. The fluctuations in “Air” temperature are also very small during this period, and C_n^2 has values almost as low as during typical sunrise and sunset transitions. Quite simply, with little net radiative forcing, the surface sensible heat flux is very small.

Once the clouds clear around 0400 hours, however, the three radiative temperatures diverge. In fact, the “IR Sky” temperature drops down to

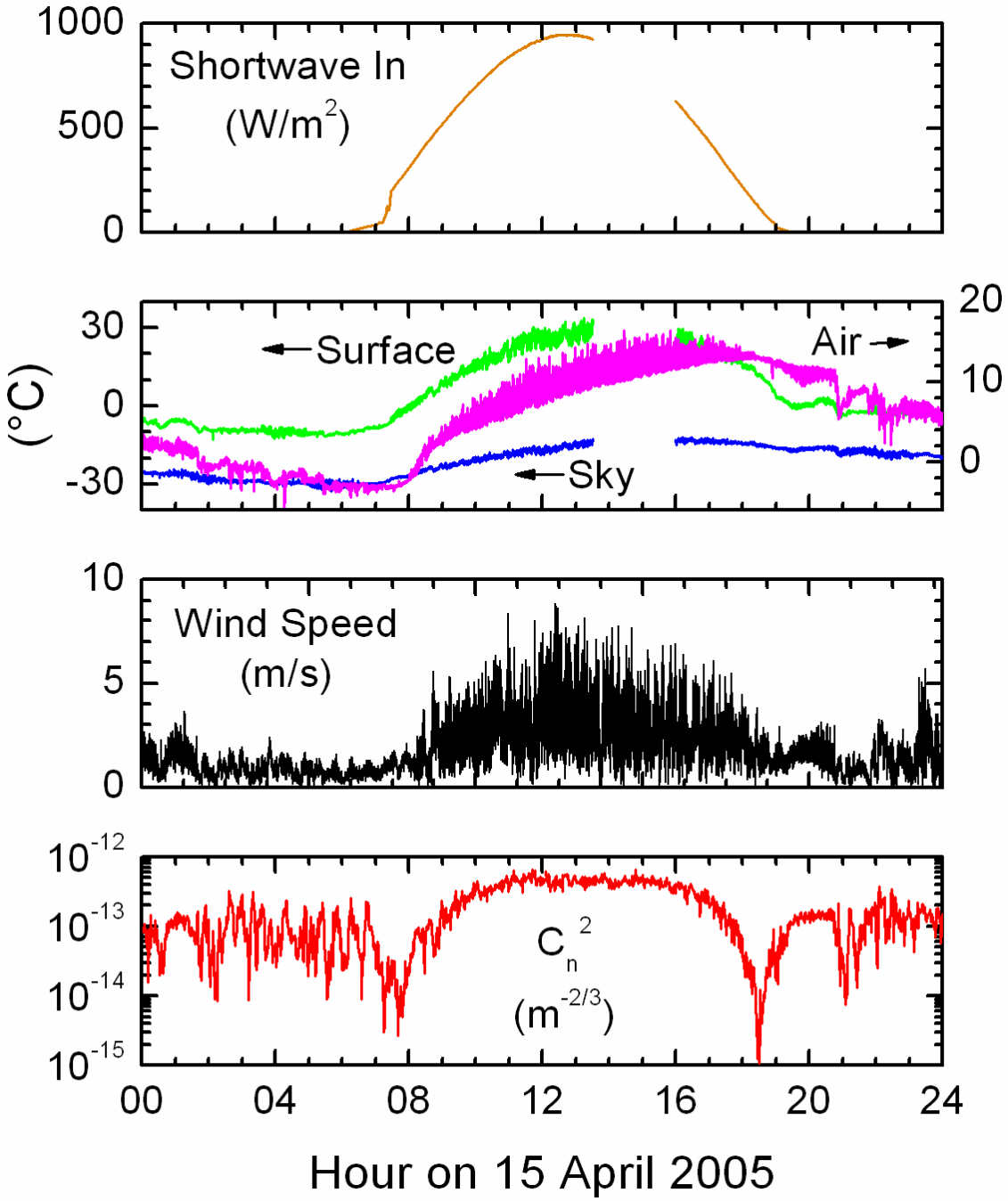

Figure 4. Time series for 15 April 2005, a day with clear skies during daylight hours. The top panel shows the incoming shortwave radiation. The second panel shows temperatures. "Surface" and "Sky" denote blackbody temperatures obtained with (1) from our downlooking and uplooking Eppley pyrgeometers, respectively. The "Air" temperature is from the sonic anemometer/thermometer. The arrows in this panel point toward the appropriate axis scale. The third panel is the wind speed from our sonic, computed as (2). The bottom panel is the refractive index structure parameter, C_n^2, from the scintillometer. Breaks in the series result from missing data.

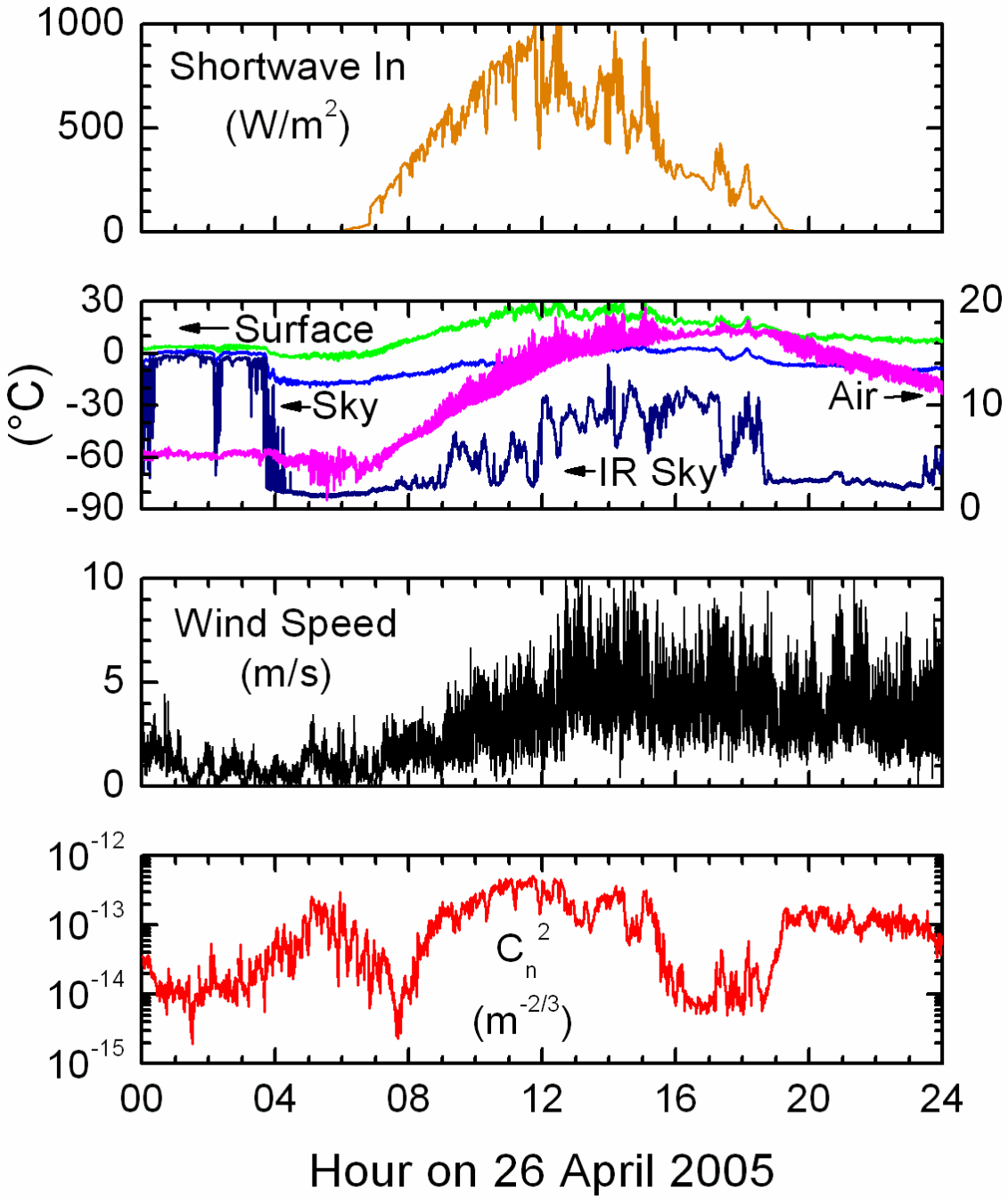

Figure 5. As in Fig. 4, except this shows 26 April 2005, a day with cloudy and clear periods. In the second panel, "IR Sky" is the blackbody temperature from our uplooking Heitronics infrared thermometer.

about –80°C, a range that we observed to be a reliable indicator of cloudless skies at this site during the experiment. By the way, the "IR Sky" temperature can be much lower than the "Sky" temperature because it comes from an instrument that has a very narrow field of view and is looking straight up. The "Sky" temperature, in contrast, comes from a hemispherical instrument that does a lot of spatial averaging, including the horizons, where the atmosphere is quite thick.

April 26 also had a lot of large and small clouds during daylight hours, as the trace of the "Shortwave In" demonstrates. These clouds are also obvious in the "IR Sky" temperature and, to a lesser extent, in the "Sky" temperature. The "Surface" temperature, "Air" temperature, and C_n^2 traces show obvious responses to this cloud forcing. Furthermore, because of the clouds preceding sunset, the usual deep evening transition in C_n^2 is not as deep and is smeared out over three hours.

The trace in "Air" temperature in Fig. 5 is closely related to the behavior of C_n^2 and reiterates the effects of cloud forcing. Between midnight and 0400 hours, when the radiative temperatures are all nearly the same, the fluctuations in "Air" temperature are small. After the clouds clear, but still before sunrise, the fluctuations in "Air" temperature increase in amplitude for about two hours but quiet down again around sunrise, when C_n^2 also goes through a minimum. During daylight, the fluctuations in "Air" temperature are 'one-sided,' upward, as warm air from the heated surface rises into cooler, baseline air. The "Air" temperature fluctuations again quiet down around sunset.

The sky clears around sunset as evidenced by the drop in "IR Sky" temperature to $-80°$ to $-90°\mathrm{C}$. After sunset, the fluctuations in "Air" temperature get large again and, again, appear one-sided. Now, though, the temperatures periodically drop from a warm baseline as the cooling surface extracts sensible heat from the warmer overlying air.

In summary, the rich texture in meteorological variables sampled at 1 Hz or faster—even on days that have long been assumed to be good for meteorological research—suggest that the assumption of stationary conditions is often invalid.

4. QUANTIFYING THE NONSTATIONARITY

One of the central issues in atmospheric turbulence is deciding how long to average a turbulence time series to obtain meaningful estimates of the mean, the variance, and the turbulent fluxes (e.g., Lumley and Panofsky 1964, p. 35ff.; Wyngaard 1973; Sreenivasan et al. 1978; Andreas 1988; Lenschow et al. 1994). Most attempts to answer this question implicitly assume that the turbulence time series is stationary. But in light of the host of time scales represented in the forcing variables in Figs. 4 and 5 and in the responses of the surface temperature and atmospheric variables, we believe that an analysis based on assuming nonstationarity may be more realistic.

Turbulence analyses typically begin with an instantaneous measurement of some variable $\tilde{x}$ (e.g., the longitudinal wind component). The purpose of averaging is to separate this instantaneous value into mean (X) and turbulence (x) components such that

$$\tilde{x} = X + x \,, \qquad (3)$$

where the average of x is zero. When a series is nonstationary, however, the mean of $\tilde{x}$ may not be approximately constant over typical hour-long averaging periods; X is thus ill-defined. The average magnitude of x may also vary. We see both manifestations of nonstationarity in the "Air" temperature and wind speed traces in Figs. 4 and 5.

Treviño and Andreas (2000), however, developed a rational way to separate the mean and the fluctuations, as required in (3), in a turbulence series that is assumed to be nonstationary. The method applies equally well to stationary series, too, though. Treviño and Andreas call their technique the Time Dependent Memory Method (TDMM; U.S. Patent No. 6,442,506) because it finds two time scales for averaging. One scale—call it ΔT—defines an averaging window over which to compute the mean (i.e., X) and, in turn, to separate the turbulent part (i.e., x). Finding ΔT requires that we specify the measurement accuracy and invoke the constraint that we cannot know something to better precision than our measurement accuracy.

A second time scale, the 'memory,' L, derives as the time implied by the autocorrelation function of the turbulent part; it is essentially an integral scale. Treviño and Andreas (2000) then take 10L as the

averaging window over which to compute the variance, $\sigma^2 = \overline{x^2}$, where the overbar indicates a time average. Usually, 10L is computed to be less than ΔT; if it is not, we set the averaging time for computing variance to ΔT.

Using this method to choose proper averaging times—even when the series is nonstationary—we can compute the mean and variance along steps through that series and can test whether the series is stationarity or nonstationary. Priestley (1981, p. 104ff.) describes the concept of a process that is stationary at order m. If a process is order-1 (first-order) stationary, its mean does not change with time. If a process is order-2 (second-order) stationary, its variance does not change with time. In Figs. 4 and 5, we see periods in the turbulence variables—"Air" temperature, wind speed, and C_n^2—for which the means and variances are changing and other periods when they are not.

Under the hypothesis that the mean is constant, the statistic

$$z = \frac{X_i - X_{i+1}}{\left[\frac{\sigma_i^2}{n_{i+1}} + \frac{\sigma_{i+1}^2}{n_i}\right]^{1/2}} \qquad (4)$$

is normally distributed with zero mean and variance 1. Here, X_i and X_{i+1} and σ_i^2 and σ_{i+1}^2 are the means and variances of adjacent intervals in a turbulence time series, computed using TDMM, and n_i and n_{i+1} are the number of independent samples used to compute the variances. By computing z, we can test for nonstationarity. If $|z|$ is larger than 1.96, say, the series is first-order nonstationary at the 95% confidence level.

Likewise, the statistic

$$F = \frac{n_i \sigma_i^2 (n_{i+1} - 1)}{n_{i+1} \sigma_{i+1}^2 (n_i - 1)} \qquad (5)$$

has an F distribution with $n_i - 1$ and $n_{n+1} - 1$ degrees of freedom. By computing F for adjacent intervals, we can test for second-order nonstationarity.

In the Time Dependent Memory Method, the averaging window for variance is generally 10L. That is, each variance estimate derives from approximately 10 independent samples since L is approximately the instantaneous correlation time of the series. Hence, n_i and n_{i+1} are both 10 in (4) and (5). Moreover, the F statistic reduces to $\sigma_i^2 / \sigma_{i+1}^2$; and in the F distribution, both degrees of freedom are 9. Hence, the 95% confidence interval for F in (5) is $[0.248, 4.03]$. F values outside this interval indicate that a time series is second-order nonstationary at better than 95% confidence.

We test these analysis ideas on five hours of the wind speed record, noon to 1700 hours, on 26 April 2005 (see Fig. 5), when the variability in the incoming shortwave radiation was extreme because of the cloud forcing. Basically, we take 10-s steps through this five-hour series and use TDMM (Treviño and Andreas 2000) to evaluate the mean and variance at each step. For this series, TDMM produced ΔT values ranging from 5 to 150 s (an imposed upper limit) and 10L values ranging from 1.3 to 343 s.

Figure 6 shows results for the hour between 1300 and 1400, when the incoming shortwave radiation varied by about 300 W m^{-2}. Figure 7 shows 1600–1700 hours, when the incoming shortwave varied by only about 100 W m^{-2}. Each figure shows the wind speed time series we used for the analysis, the resulting z and F statistics computed from (4) and (5) after we used TDMM to separate mean and turbulent parts of the series, and the 95% confidence intervals for z and F. Remember, our interpretation of the z and F values is that points outside these confidence intervals indicate a high probability of nonstationary behavior.

Although the shortwave forcing was dramatically different during the periods covered by Figs. 6 and 7, both figures show a high incidence of nonstationary behavior. In Fig. 6, 12% of the z values and 14% of the F values are outside the 95% confidence intervals. In Fig. 7, 20% of the z values and 21% of the F values are outside the confidence intervals. For the five total hours that we analyzed from 26 April, 1200–1700 hours, these numbers are typical: The z values during each hour were outside the 95% confidence interval from 12% to 21% of the time, and the F values during each hour were outside the 95% confidence interval from 14% to 26% of the time. If this wind speed series were both first-order and second-order stationary with 95% confidence during these five hours, we would expect only 5% of the z and F statistics to be outside the 95% confidence intervals. Thus, we judge the entire five hours between noon and 1700 hours on April 26 as nonstationary.

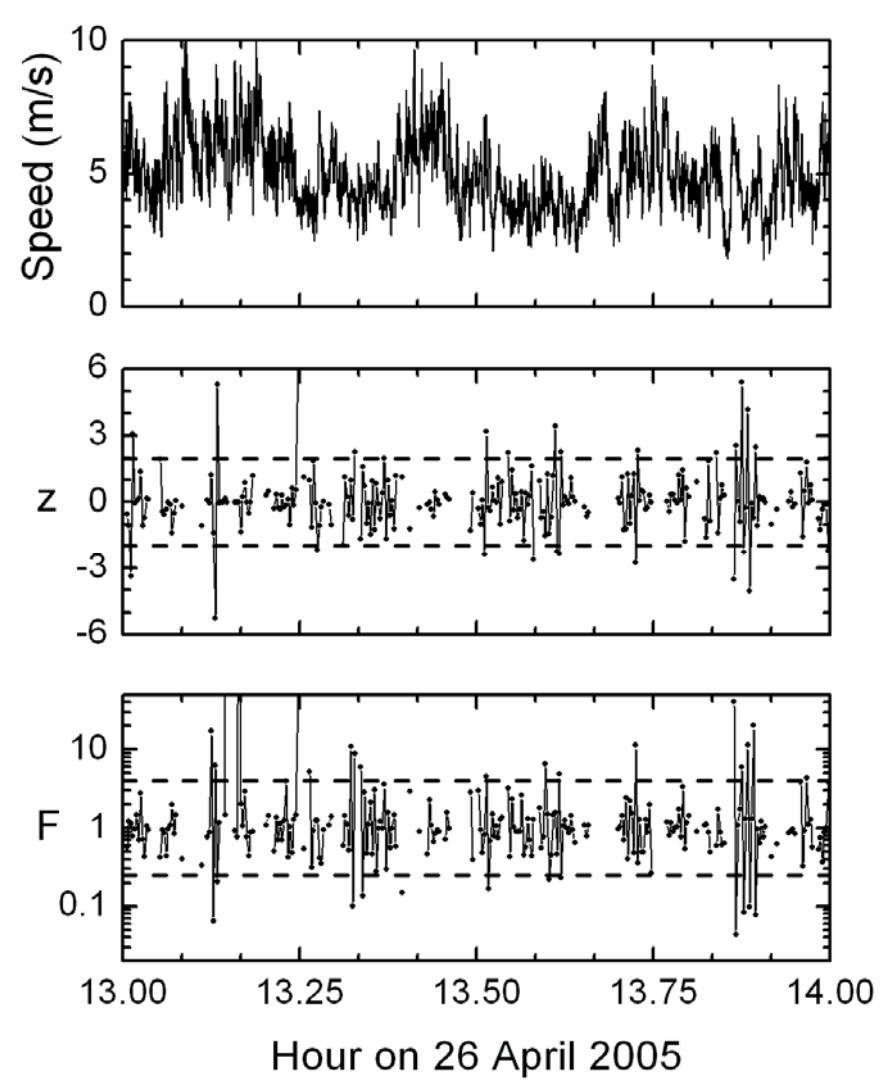

Figure 6. Time series of wind speed and the z [from (4)] and F [from (5)] statistics for the wind speed for 1300–1400 hours on 26 April 2005. Dashed lines in the z and F panels show the 95% confidence limits. Breaks in the z and F series result from missing data or our failure to find a reliable averaging period.

Another conclusion we reach on viewing Figs. 6 and 7 and considering the numbers given above is that, for these five hours, the wind speed series displays slightly more second-order than first-order nonstationarity. Quite simply, in Figs. 6 and 7 and for the other three hours not shown, the z statistic is within its 95% confidence band more often than the F statistics is within its confidence band.

If we study Figs. 6 and 7 in detail, we can see what information the TDMM calculations are yielding and that our tests of the z and F statistics are producing the results we anticipate. First, we chose the periods 1300–1400 hours and 1600–1700 hours because they correspond with periods of high and relatively low solar forcing, respectively. But our analyses in Figs. 6 and 7 seem to suggest that the wind speed is not responding strongly to this forcing: Fig. 6 exhibits less nonstationarity than Fig. 7.

We do see in the two figures, though, that first-order and second-order nonstationarity tends to go hand-in-hand. That is, excursions in the z statistic outside of its 95% confidence band correspond with excursions in the F statistic

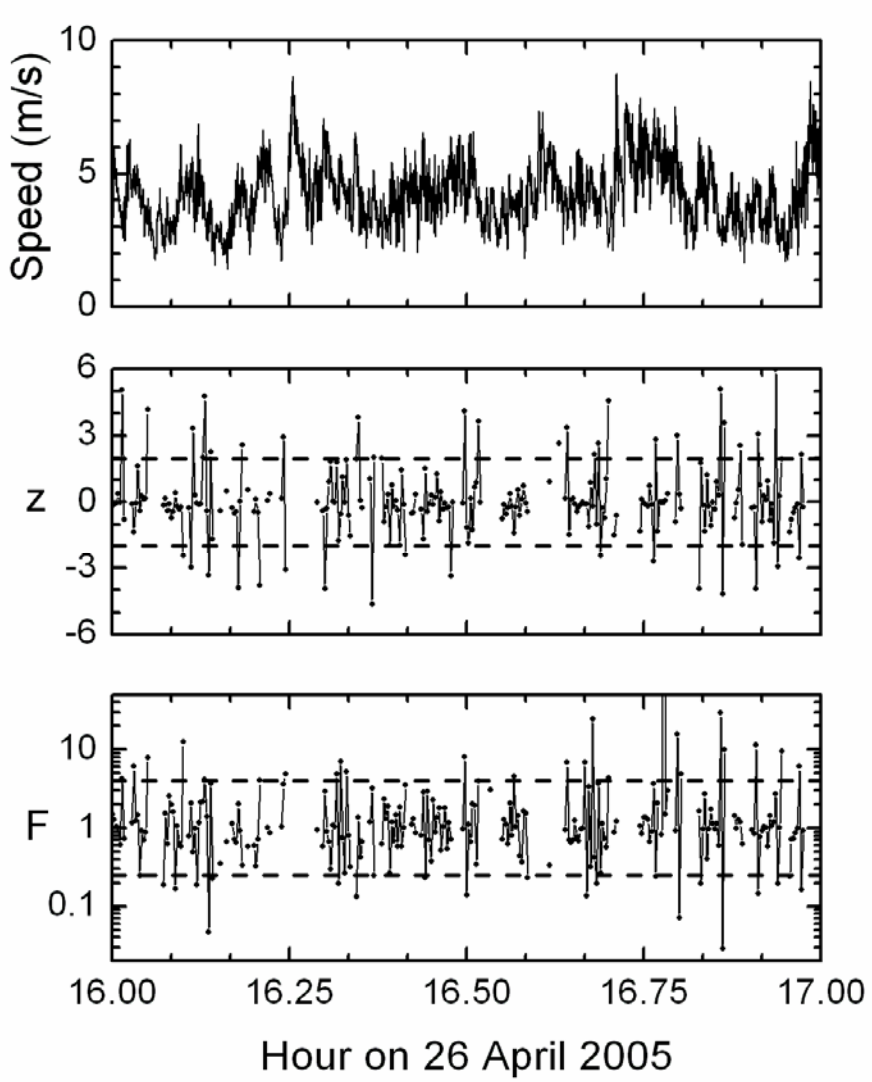

Figure 7. As in Fig. 6, except for 1600–1700 hours on 26 April 2005.

outside of its 95% confidence band. For example, the period in Fig. 6 from about 13.80 to 13.90 hours features large, coherent oscillations in the wind speed that result in simultaneously extreme values of the z and F statistics.

This clustering of nonstationary events is rather typical of Fig. 6. It shows other such nonstationary events at 13.10–13.20 hours and at 13.50–13.60 hours. In Fig. 7, in contrast, the nonstationarity is distributed pretty uniformly throughout the time series. Thus, we might say that the wind speed series in Fig. 6 shows 'bursty' events, while the wind speed series in Fig. 7 is more randomly variable. Compare similar descriptions of nonstationary time series in Mahrt (1998) and Andreas et al. (2003).

5. CONCLUSIONS

We have tried to highlight some of the surface and near-surface atmospheric effects that we plan to study with the data we collected in April 2005. Our first hypothesis in analyzing these data is that all near-surface variables are closely coupled over very short time scales because all respond to the same forcing by incoming shortwave and longwave radiation. Our second hypothesis is that near-surface atmospheric processes are often nonstationary because of changes in this forcing. Quantifying nonstationarity is therefore essential to our analysis.

We have thus devised a new, quantitative method for characterizing nonstationarity and have

demonstrated that method with a five-hour time series of wind speed (Figs. 6 and 7). First, we use the Time Dependent Memory Method (Treviño and Andreas 2000) to calculate X_i and σ_i every 10 s. Next, we compute z and F statistics between consecutive time steps to test for first-order and second-order stationarity, respectively. We found each hour during this five-hour example to be first-order nonstationary between 12% and 21% of the time with 95% confidence and to be second-order nonstationary between 14% and 26% of the time.

The only similar attempt at a quantitative evaluation of nonstationarity that we know of is Mahrt's (1998) nonstationarity ratio. Evaluating it, though, requires some arbitrary choices of averaging intervals, and the resulting ratio depends on these choices (Andreas et al. 2003). Furthermore, Mahrt gave only a qualitative appraisal of how to interpret his nonstationarity ratio.

Our method, on the other hand, uses TDMM to decide how best to average a series to separate mean and turbulent parts. We then compute two statistics, z and F, which have well known statistical properties and for which we can thus assign confidence limits. Consequently, we can judge quantitatively whether a series exhibits first-order or second-order nonstationarity.

One problem we ran into in using the TDMM algorithm in this, our first extensive test with it, is that it produced a suitable ΔT for separating mean and turbulent components only 73% of the time. We can probably improve this performance by extending the maximum length of the sample to which we apply TDMM—currently limited to 150 s—or by decreasing the presumed measurement precision—currently set at $\pm 0.03\sqrt{3}\,\mathrm{m\,s^{-1}}$. In the near future, we will therefore be evaluating how these few arbitrary parameters in TDMM control its performance.

6. ACKNOWLEDGMENTS

The U.S. Department of the Army supported this work through Project 611102T2400.

7. REFERENCES

Andreas, E. L, 1988: Estimating averaging times for point and path-averaged measurements of turbulence spectra. *J. Appl. Meteor.,* **27**, 295-304.

____, 1989: Two-wavelength method of measuring path-averaged turbulent surface heat fluxes. *J. Atmos. Oceanic Technol.*, **6**, 280–292.

____, 1991: Using scintillation at two wavelengths to measure path-averaged heat fluxes in free convection. *Bound.-Layer Meteor.*, **54**, 167–182.

____, 1992: Uncertainty in a path-averaged measurement of the friction velocity u_*. *J. Appl. Meteor.*, **31**, 1312-1321.

____, R. J. Hill, J. R. Gosz, D. I. Moore, W. D. Otto, and A. D. Sarma, 1998: Statistics of surface-layer turbulence over terrain with metre-scale heterogeneity. *Bound.-Layer Meteor.*, **86**, 379–408.

____, C. W. Fairall, P. O. G. Persson, and P. S. Guest, 2003: Probability distributions for the inner scale and the refractive index structure parameter and their implications for flux averaging. *J. Appl. Meteor.*, **42**, 1316–1329.

De Bruin, H. A. R., W. M. L. Meijninger, A.-S. Smedman, and M. Magnusson, 2002: Displaced-beam small aperture scintillometer test. Part I: The WINTEX data-set. *Bound.-Layer Meteor.*, **105**, 129–148.

Hill, R. J., 1992: Review of optical scintillation methods of measuring the refractive-index spectrum, inner scale and surface fluxes. *Waves in Random Media*, **2**, 179–201.

____, and S. F. Clifford, 1978: Modified spectrum of atmospheric temperature fluctuations and its application to optical propagation. *J. Opt. Soc. Amer.*, **68**, 892–899.

____, G. R. Ochs, and J. J. Wilson, 1992: Measuring surface-layer fluxes of heat and momentum using optical scintillation. *Bound.-Layer Meteor.*, **58**, 391–408.

Kaimal, J. C., and J. J. Finnigan, 1994: *Atmospheric Boundary Layers Flows: Their Structure and Measurement*. Oxford University Press, 289 pp.

____, and J. E. Gaynor, 1991: Another look at sonic thermometry. *Bound.-Layer Meteor.*, **56**, 401–410.

____, ____, H. A. Zimmerman, and G. A. Zimmerman, 1990: Minimizing flow distortion errors in a sonic anemometer. *Bound.-Layer Meteor.*, **53**, 103–115.

Kristensen, L., J. Mann, S. P. Oncley, and J. C. Wyngaard, 1997: How close is close enough when measuring scalar fluxes with displaced sensors? *J. Atmos. Oceanic Technol.*, **14**, 814–821.

Kukharets, V. P., and L. R. Tsvang, 1998: Atmospheric turbulence characteristics over a

temperature-inhomogeneous land surface. Part I: Statistical characteristics of small-scale spatial inhomogeneities of land surface temperature. *Bound.-Layer Meteor.*, **86**, 89–101.

Lenschow, D. H., J. Mann, and L. Kristensen, 1994: How long is long enough when measuring fluxes and other turbulence statistics? *J. Atmos. Oceanic Technol.*, **11**, 661–673.

Lumley, J. L., and H. A. Panofsky, 1964: *The Structure of Atmospheric Turbulence.* Interscience, 239 pp.

Mahrt, L., 1998: Flux sampling errors for aircraft and towers. *J. Atmos. Oceanic Technol.*, **15**, 416–429.

Priestley, M. B., 1981: *Spectral Analysis and Time Series.* Academic Press, 890 pp.

Roth, M., and T. R. Oke, 1995: Relative efficiencies of turbulent transfer of heat, mass, and momentum over a patchy urban surface. *J. Atmos. Sci.*, **52**, 1863–1874.

Sreenivasan, K. R., A. J. Chambers, and R. A. Antonia, 1978: Accuracy of moments of velocity and scalar fluctuations in the atmospheric surface layer. *Bound.-Layer Meteor.*, **14**, 341–359.

Thiermann, V., 1992: A displaced-beam scintillometer for line-averaged measurements of surface layer turbulence. Preprints, *Tenth Symp. on Turbulence and Diffusion*, Portland, OR, Amer. Meteor. Soc., 244–247.

Treviño, G., and E. L Andreas, 2000: Averaging intervals for spectral analysis of nonstationary turbulence. *Bound.-Layer Meteor.*, **95**, 231–247.

Wyngaard, J. C., 1973: On surface-layer turbulence. *Workshop on Micrometeorology*, D. A. Haugen, Ed., Amer. Meteor. Soc., 101–149.